Miner Deposita (2015) 50:643–656
DOI 10.1007/s00126-015-0597-9

LETTER

Extreme variation of sulfur isotopic compositions in pyrite from the Qiuling sediment-hosted gold deposit, West Qinling orogen, central China: an in situ SIMS study with implications for the source of sulfur

Lei Chen[1] · Xian-hua Li[1] · Jian-wei Li[2] · Albert H. Hofstra[3] · Yu Liu[1] · Alan E. Koenig[3]

Received: 28 November 2014 / Accepted: 29 May 2015 / Published online: 19 June 2015

Abstract High spatial resolution textural (scanning electron microscope (SEM)), chemical (electron microprobe (EMP)) and laser ablation-inductively coupled plasma-mass spectrometry (LA-ICP-MS)), and sulfur isotopic (secondary ion mass spectrometry (SIMS)) analyses of pyrite from the Qiuling sediment-hosted gold deposit (232±4 Ma) in the West Qinling orogen, central China were conducted to distinguish pyrite types and gain insights into the source and evolution of sulfur in hydrothermal fluids. The results reveal an enormous variation (−27.1 to +69.6‰) in sulfur isotopic composition of pyrite deposited during three paragenetic stages. Pre-ore framboidal pyrite, which is characterized by low concentrations of As, Au, Cu, Co, and Ni, has negative $\delta^{34}S$ values of −27.1 to −7.6‰ that are interpreted in terms of bacterial reduction of marine sulfate during sedimentation and diagenesis of the Paleozoic carbonate and clastic sequences, the predominant lithologies in the deposit area, and the most important hosts of many sediment-hosted gold deposits throughout the West Qinling orogen. The ore-stage hydrothermal pyrite contains high concentrations of Au, As, Cu, Sb, Tl, and Bi and has a relatively narrow range of positive $\delta^{34}S$ values ranging from +8.1 to +15.2‰. The sulfur isotope data are comparable to those of ore pyrite from many Triassic orogenic gold deposits and Paleozoic sedimentary exhalative (SEDEX) Pb-Zn deposits in the West Qinling orogen, both being hosted mainly in the Devonian sequence. This similarity indicates that sulfur, responsible for the auriferous pyrite at Qiuling, was largely derived from the metamorphic devolatization of Paleozoic marine sedimentary rocks. Post-ore-stage pyrite, which is significantly enriched in Co and Ni but depleted in Au and As, has unusually high $\delta^{34}S$ values ranging from +37.4 to +69.6 ‰, that are interpreted to result from thermochemical reduction of evaporite sulfates in underlying Cambrian sedimentary rocks with very high $\delta^{34}S$ values. The variations in Au content and sulfur isotopic compositions across a single ore-stage pyrite grain may reflect displacement of indigenous groundwater with low $\delta^{34}S$ values by auriferous metamorphic fluids with high $\delta^{34}S$ values. The very low-grade metamorphism of the host rocks and the metamorphic derivation of sulfur for the ore pyrite indicate that the Qiuling sediment-hosted gold deposit is an epizonal manifestation of an orogenic gold system in the West Qinling orogen.

Keywords Pyrite · SIMS · Sulfur isotopes · Sediment-hosted gold deposit · Qinling orogen

Editorial handling: R. Hu

Electronic supplementary material The online version of this article (doi:10.1007/s00126-015-0597-9) contains supplementary material, which is available to authorized users.

✉ Lei Chen
chenlei1211@mail.iggcas.ac.cn; chenlei1211@gmail.com

[1] State Key Laboratory of Lithospheric Evolution, Institute of Geology and Geophysics, Chinese Academy of Sciences, Beijing 100029, China

[2] State Key Laboratory of Geological Processes and Mineral Resources, China University of Geosciences, Wuhan 430074, China

[3] U.S. Geological Survey, MS 973, Denver, CO 80225, USA

Introduction

Sediment-hosted disseminated gold deposits are currently the world's largest source of gold (Saunders et al. 2014). These comprise Carlin-type gold deposits (Cline et al. 2005) and orogenic varieties (Large et al. 2011). In these deposits, gold is transported as bisulfide complexes in acidic hydrothermal fluids and coprecipitates with pyrite or arsenopyrite (Hofstra

et al. 1991; Hofstra and Cline 2000; Emsbo et al. 2003; Groves et al. 2003; Goldfarb et al. 2005; Large et al. 2007, 2009, 2011). Therefore, knowledge of the sulfur isotopic composition of auriferous pyrite is a key to advance understanding of the source of reduced sulfur and, by inference, gold in the ore-forming fluids (Kesler et al. 2005; Chang et al. 2008).

Gold-bearing pyrite in sediment-hosted disseminated gold deposits is typically fine-grained, texturally complex, and enriched in As, Sb, Tl, Hg, and Cu, and it frequently occurs with older and younger generations of pyrite in the ores (Cline et al. 2005; Large et al. 2007, 2009, 2011). For samples with texturally complex pyrite, conventional methods that analyze bulk ore samples or pyrite separates generally are unable to precisely characterize the chemical or sulfur isotopic composition of ore-stage pyrite. Consequently, data obtained using conventional methods generally is not as geologically meaningful or definitive as that obtained by microanalysis (e.g., SIMS, LA-ICP-MS).

The West Qinling orogen in central China hosts numerous sediment-hosted gold deposits and is one of the largest gold-producing areas in the country (Mao et al. 2002; Chen et al. 2004). Several important sediment-hosted gold deposits, such as Qiuling, are present on the southern flank of the West Qinling orogen and are mostly hosted in Devonian and Carboniferous marine clastic and carbonate rocks. Pyrite and arsenopyrite are the most important gold-bearing minerals in these deposits. At Qiuling, field and petrographic observations have revealed three types of pyrite: framboidal pyrite in the host rocks, fine-grained pyrite with spectacular zoning structure in gold ores, and coarse-grained pyrite in quartz veinlets cutting gold ores. In this paper, we present an EMP major element, LA-ICP-MS trace element, and SIMS sulfur isotope analyses of the three types of pyrite as well as different zones in single fine-grained auriferous and coarse-grained barren pyrite grains. Combined with other regional data, the results are used to identify possible sources of sulfur during each stage of pyrite formation. The micrometer-scale chemical and isotopic variations in ore and post-ore pyrite are also used to constrain ore-forming processes.

Geological background

Geology of the West Qinling orogen

The roughly east-west striking Qinling orogen formed by continental collision of the Yangtze and North China cratons in the Middle-Late Triassic (Fig. 1a; Dong et al. 2011). The Qinling orogen has been traditionally divided into the North Qinling and South Qinling belts that are separated by the Shangdan suture, which is formed by the subduction and closure of the Early Paleozoic Shangdan Ocean in the Late Devonian (Fig. 1b; Zhang et al. 2001; Ratschbacher et al. 2003; Dong et al. 2011). The South Qinling belt is bounded by the Yangtze craton along the A'nemaqen-Mianlue suture that is formed by subduction and closure of the A'nemaqen and Mianlue portions of the Paleo-Tethys Ocean in the Early-Middle Triassic (Dong et al. 1999; Zhang et al. 2001).

The South Qinling belt is underlain by Paleo- to Mesoproterozoic basement metamorphic complex composed of paragneiss and marble that is overlain by low-K tholeiite to calc-alkaline and alkaline basalts with arc signatures (Zhang et al. 2000). They are unconformably overlain by Cambrian to Triassic marine sedimentary rocks with a maximum thickness of 12,000 m. The northern part of South Qinling belt is characterized by a highly deformed basinal flysch sequence (Xue et al. 1996; Lai et al. 1998), with the Fengxian-Zhen'an Fault as boundary (Fig. 1b). The flysch consists mainly of Devonian clastic and carbonate rocks with minor Carboniferous and Permian metasedimentary rocks in places, and was metamorphosed to sub-greenschist to greenschist facies during the Triassic orogeny (Zhai et al. 1998; Goldfarb et al. 2014). To the south of the Fengxian-Zhen'an Fault, extensive Devonian strata are overlain by Triassic turbidites with small local Cambrian to Ordovician sedimentary rocks in the middle and west, which portray the Zipper Suturing model (Fig. 1c). The Cambrian contains a distinctive sequence of sediments composed of pyritic black shale, black chert, and carbonate rock. Organic carbon contents are generally more than 1 wt%. Characteristic lithologies are black chert (thick and thin bedded), phosphatic concretions, barite (in most places), witherite and barytocalcite (in a few places), and black shales, with a total thickness of 1000 m (Wang and Li 1991). The Lower Cambrian carbonaceous rocks are characterized by enrichment in V, U, Ni, Mo, Fe, P, REE, Se, stone coal, and locally Au, and most rocks also show some degree of Ba enrichment (Wang and Li 1991). The La'erma and Qiongmo Au-Se deposits are the best representative of gold mineralization in the Lower Cambrian carbonaceous rocks (Liu et al. 2000). Silurian to Devonian rocks are dominated by a flysch sequence consisting of meta-graywacke, slate, phyllite, and carbonate that is indicative of significant subsidence and rapid sedimentation (Zhang 1988). Most of the gold deposits in the South Qinling belt are hosted in Devonian rocks composed of carbonate, siliciclastic, and argillaceous rocks with a total thickness of ca. 3000 to 8000 m that were deposited in several growth fault-bounded basins (Liu et al. 1990). Numerous sedimentary exhalative (SEDEX) Pb-Zn sulfide deposits have been recognized in the Devonian rocks (Fig. 1c; Qi and Li 1993). The Devonian sequence is conformably overlain by Carboniferous to Triassic rocks consisting of shallow marine limestone with minor amounts of siliciclastic sediment and, locally, coal (Ma et al. 2004, 2007).

The Paleozoic and Triassic sedimentary rocks were intensely deformed during the Middle to Late Triassic Qinling orogeny that produced numerous regional northwestern striking folds and associated thrust faults extending for a few tens to hundreds of kilometers along strike (Fig. 1b). These faults and their

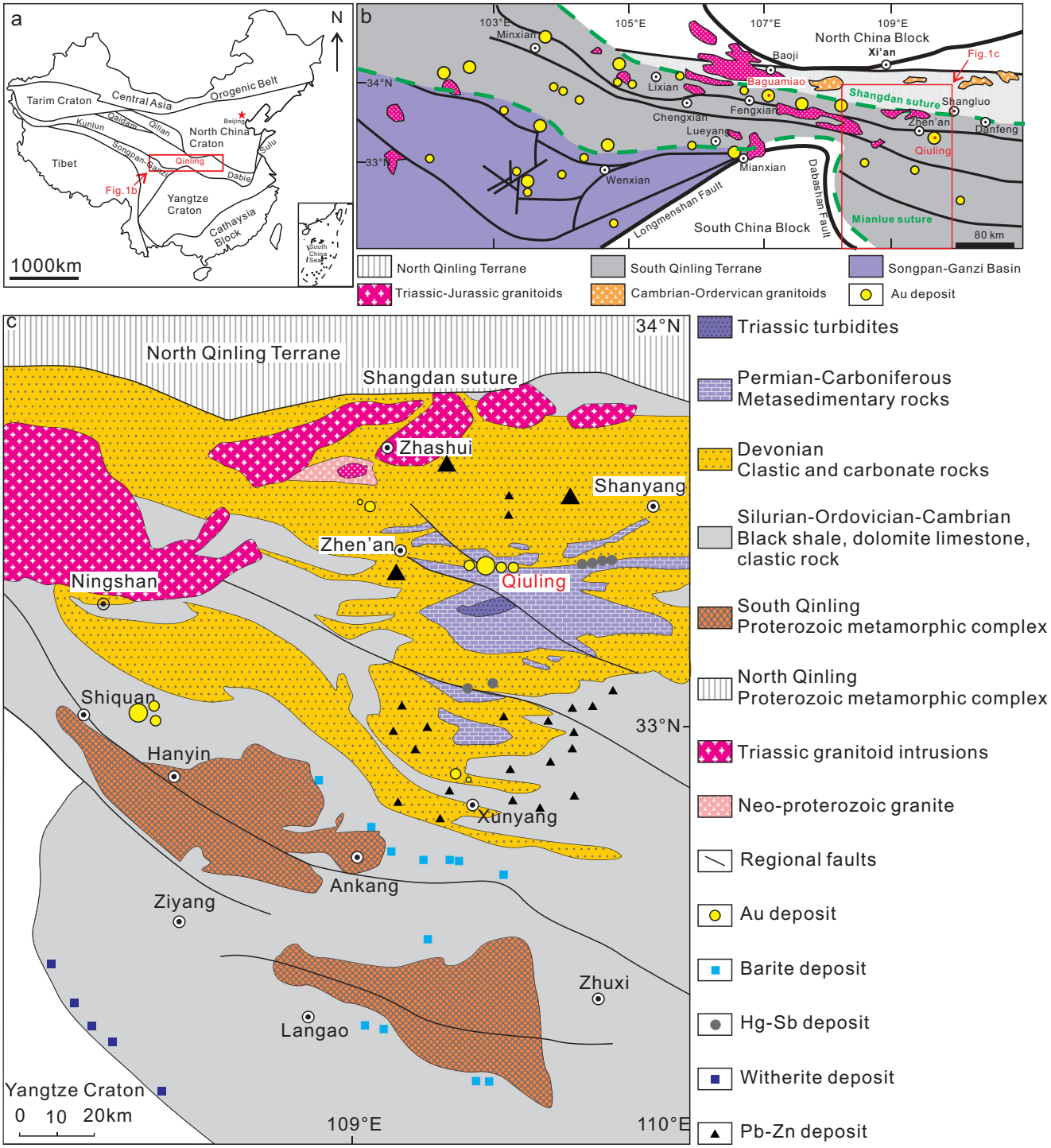

Fig. 1 **a** Tectonic division of China showing the Qinling orogen between the Yangtze and North China cratons. **b** Sketch geologic map of the West Qinling orogen showing the location of major gold deposits relative to regional faults and granitoid intrusions (modified after Chen et al. 2004). **c** Simplified geologic map of the southern segment of the West Qinling orogenic belt where Qiuling is located

subsidiary structures control the distribution of gold deposits in the West Qinling orogen (Mao et al. 2002; Chen et al. 2004).

Numerous granitoid intrusions are present in the Devonian sequences to the south of the Shangdan suture (Fig. 1c). These granitoid rocks were emplaced during closure of the Mianlue Ocean and the ensuing collision between the Yangtze and North China cratons (Qin et al. 2009). Based on emplacement ages and geochemical data, both syn-collisional and post-collisional granitoid intrusions have been recognized. The syn-collisional intrusions formed between 239 and 217 Ma (Dong et al. 2011 and references therein). Many intrusions have high-K calc-alkaline compositions and are enriched in large

iron lithophile elements and light rare earth elements but depleted in high field strength elements and heavy rare earth elements (Dong et al. 2011). The post-collisional intrusions were emplaced between 217 and 200 Ma in an extensional setting as indicated by the rapakivi textures and mafic microgranular enclaves and mafic dikes present in many granitoid intrusions (Zhang et al. 2008; Qin et al. 2009; Wang et al. 2011).

Geology of the Qiuling gold deposit

The Qiuling gold deposit is located in the southern belt of the West Qinling orogen (Fig. 1c). Gold mineralization is hosted mainly in the Upper Devonian Nanyangshan and Lower Carboniferous Yuanjiagou Formations, which variably consist of pyritic black shale, siltstone, argillaceous siltstone, and limestone with no or very low-grade metamorphism (Fig. 2). Pyrite is abundant in the black shales and siltstones and commonly displays framboidal textures (Zhang et al. 1993). The Devonian and Carboniferous sedimentary rocks have been slightly metamorphosed to sub-greenschist facies during the Triassic orogenesis involving the collision between the Yangtze and North China craton. The orogenic deformation has led to the formation of a number of faults and folds involving the Paleozoic sequence, which occurs mostly along a northwestern or nearly east-western strike and have been overprinted by NE- to NNE-striking faults (Fig. 2a). The WNW-striking

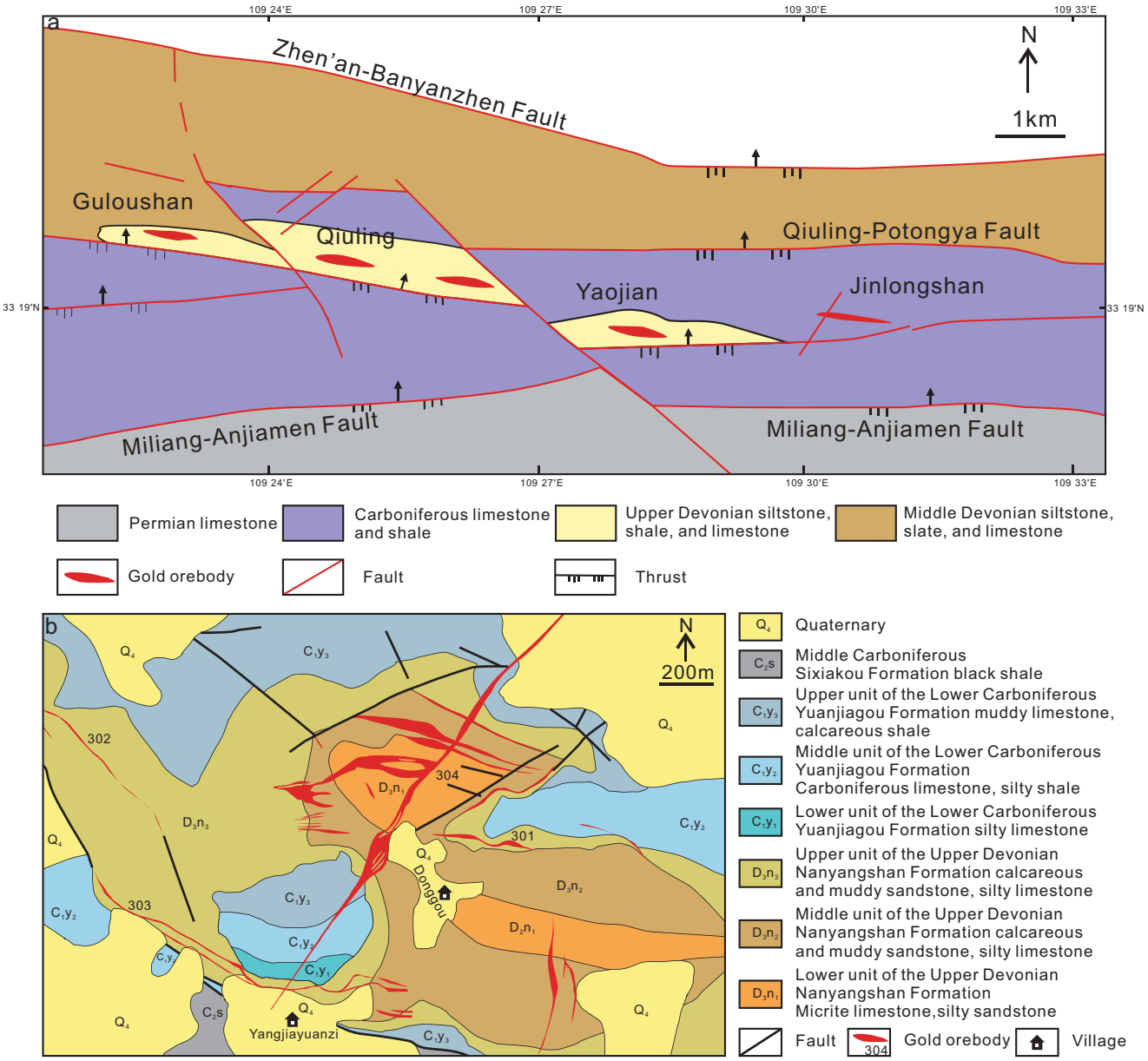

Fig. 2 **a** Geological sketch map of the location of the Qiuling gold deposit (after Zhang et al. 1993). **b** Geological map of the Qiuling sediment-hosted gold deposit (after Hua 2012)

Qiuling anticline is the principal structural feature in the mine. A number of subsidiary folds are present in the northern limb of the Qiuling anticline. Although NE- and WNW-striking faults are present in the mining area (Fig. 2b), gold ore bodies are mainly hosted in WNW-striking transpressional faults. No igneous rocks are exposed in the area.

The Qiuling gold deposit consists of five ore bodies (301, 302, 303, 304, and 308) with strike length of 180–974 m and thickness of 0.7–46 m (Fig. 2b). Together they have a proven reserve of 50 t Au at an average grade of 3–4 g/t gold (Hua et al. 2012). Gold mineralization is dominated by disseminations of fine-grained auriferous pyrite and arsenopyrite in carbonaceous shales and siltstones, with minor amounts of veinlets composed of coarse-grained pyrite, arsenopyrite, and quartz. Quartz-stibnite veins are locally present, commonly overprinting the pyrite and arsenopyrite disseminations. Other minor to trace metallic minerals are sphalerite, chalcopyrite, and galena. Ore-related gangue minerals include quartz, calcite, sericite, and ankerite. Hydrothermal alteration is pervasive and involves a combination of silicification, sericitization, carbonatization, and decarbonization. Samnium-strontium dating of hydrothermal calcite from high-grade ores yielded an isochron age of 232±4 Ma (Hua 2012), indicating that the Qiuling gold deposits formed coevally with the Triassic orogeny forming the Qinling orogen.

Samples and analytical methods

Samples and preparation

Eight samples were collected for this study. Samples QL102 and QL105 were taken from the 301 ore body, whereas samples QL110, QL112, QL113, QL114, QL116, and QL122 were selected from the 304 ore body. Each sample was prepared as polished thick sections and was examined under optical microscopy to characterize the mineralogy, morphology, and textures of pyrite. Areas (3~5 mm diameter) of the thick sections containing multiple types of pyrite were cut out with a micro drill and mounted in 25-mm diameter epoxy discs together with pieces of pyrite standards for SIMS sulfur isotope analysis. The standards used in this study were Sonora pyrite and Balmat pyrite (Crowe and Vaughan 1996; Farquhar et al. 2013). The discs were polished to produce a smooth, flat sample surface with relief less than a few micrometer, which is critical for high-accuracy, high-precision isotope ratio analysis by SIMS (Kita et al. 2011). After SIMS sulfur isotope analysis, the discs were used for compositional analysis.

Occurrence and texture of pyrite

Three types of pyrite were recognized in the studied samples. Type 1 pyrite (Py1) typically has framboidal textures consisting of roughly spherical aggregates, 10 to 20 μm in diameter, that are comprised of euhedral microcrystallites less than 1 to 5 μm in size (Fig. 3a). Framboidal pyrite not only occurs mostly in black shales and siltstones of the Nanyangshan Formation but also is common in gold ores. Type 2 pyrite (Py2) is euhedral and fine-grained, ranging in size from <10 to 50 μm (Fig. 3b). It commonly coexists with arsenopyrite in strongly altered and mineralized rocks of the Nanyangshan and Yuanjiagou Formations. Backscattered electron images show that Py2 consists of dark cores and zoned rims (Fig. 3b). Type 3 pyrite (Py3) is coarse-grained and generally more than 100 μm in size. It forms veinlets with quartz cutting gold ores in hydrothermally altered rocks of the Nanyangshan Formation (Fig. 3c).

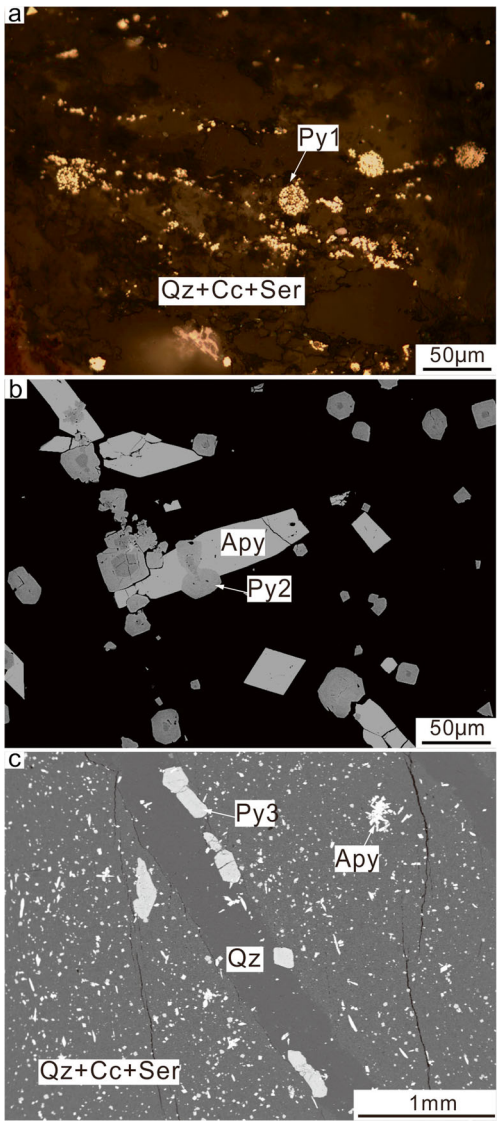

Fig. 3 **a** Reflected-light photograph of Py1 framboids in clastics layer within the Upper Devonian Nanyangshan Formation. **b** Backscattered electron image of main ore-stage-zoned Py2 and arsenopyrite. **c** Backscattered electron image of post-ore-stage coarse euhedral Py3. Mineral abbreviations: *Py* pyrite, *Qz* quartz, *Cc* calcite, *Ser* sericite, *Apy* arsenopyrite

Textural and compositional analysis

After petrographic examination, the samples were investigated using scanning electron microscopy to characterize the morphological and textural features of pyrite grains. Samples were coated with a 250-Å carbon film and then imaged using a Quanta 200 scanning electron microscope with secondary electron imaging (SEI) and backscattered electron (BSE) modes. The EDAX GENESIS energy-dispersive spectroscopy (EDS) was performed using an accelerating voltage of 15 kV and a working distance of 11 mm.

Major elements were analyzed using a JEOL JXA-8100 microprobe with fully automated five X-ray wavelength dispersive spectrometers (WDS). The operating conditions consisted of an acceleration voltage of 15 kV, a probe current of 20 nA, and a beam diameter of 5 μm. The following sulfides were used as standards: FeS_2 (Fe, S), FeAsS (As), PbS (Pb), $CuFeS_2$ (Cu), ZnS (S), NiS (Ni), and CoS (Co). The detection limits for each element were Fe (126 ppm), S (126 ppm), As (478 ppm), Pb (616 ppm), Cu (111 ppm), Zn (189 ppm), Ni (96 ppm), and Co (88 ppm).

Trace elements (As, Cu, Pb, Sb, Au, Ag, Bi, Tl, Co, and Ni) were analyzed using laser ablation-inductively coupled plasma-mass spectrometry (LA-ICP-MS) at the U.S. Geological Survey, Denver Federal Center. Quantitative trace element data were obtained using a Perkin-Elmer Sciex ELAN 6000 quadrupole mass spectrometer attached to a CETAC LSX500 laser system. The analyses were performed in spot mode using a laser beam of 30 μm diameter and a repetition rate of 5 Hz. The energy density was 5 J/cm^2, and the ablated materials were transported to the ICP-MS in a stream of helium (combined flow of 1.0 L/min). Data were collected in the time-resolved mode. Each analysis incorporated a background acquisition of 30 s (gas blank) followed by 60 s data acquisition. All analyses were quantified against USGS synthetic MASS-1 standard (Wilson et al. 2002), following the procedure of Longerich et al. (1996) and using Fe as the internal standard. The detection limits for each element were Au (0.90 ppm), Ag (2.26 ppm), Co (3.18 ppm), Ni (8.48 ppm), Cu (12.34 ppm), As (45 ppm), Sb (7.02 ppm), Tl (0.79 ppm), Pb (8.09 ppm), and Bi (0.56 ppm).

Sulfur isotope analysis

In situ sulfur isotope (^{32}S, ^{33}S, and ^{34}S) analyses were performed using a Cameca IMS-1280 at the Institute of Geology and Geophysics (Beijing), Chinese Academy of Sciences. Detailed SEI and BSE images were utilized to select spots for analysis and to avoid defects and contamination from other phases. The Cs^+ primary ion beam was accelerated at 10 kV, with an intensity of ca. 2.5 nA (Gaussian mode with a primary beam aperture of 400 μm to reduce aberrations). The beam was scanned ~25×25 μm during analysis to reduce the depth of crater.

Although the samples are conductive, the normal-incidence electron flood gun (NEG) was used to neutralize the possible positive charge buildup in the analysis area. Negative secondary ions were extracted with a −10-kV potential. The field aperture was set to 2000 μm, and the transfer-optics magnification was adjusted to give a field of view of 125 μm (FA=8000). Energy slit width was 25 eV; the mechanical position of the energy slit was calibrated before starting the session (5 eV gap with respect to the maximum). Sulfur isotopes were measured in multi-collector mode using three off-axis Faraday cups (L'2, L1, and H1), using an entrance slit width of 60 μm and exit slit width of 500 μm on each of three Faraday cup detectors positioned along the focal plane for simultaneous measurement of ^{32}S, ^{33}S, and ^{34}S. For most of analytical sessions reported, the high mass resolution power (MRP) (>~4000) was sufficient to resolve ^{33}S from $^{32}S^1H$ (Mojzsis et al. 2003; Whitehouse et al. 2005). However, a poor peak shape for mass ^{32}S (ESM 1a) will arise from the outer position of the L'2 cup relative to the optical axis of the ion beam. In this study, a MRP of 2400 was employed to have flat top peaks on all the masses. A step-shaped peak was obtained, with ^{33}S peak on the left and $^{32}S^1H$ peak on the right (ESM 1b). Both steps have sufficient flat plateau to set the magnetic field. The magnetic field was centered by the other two mass peaks, and the L1 detector was moved to the center of the ^{33}S plateau. A stable magnetic field was maintained using nuclear magnetic resonance (NMR) regulation. The intensity of ^{32}S was typically 1×10^9 cps. Each analysis takes about 4.5 min, consisting of 30 s pre-sputtering, 60 s of automated centering of secondary ions, and 160 s integrating sulfur isotope signals (40 cycles×4 s).

Sonora pyrite was used as a running standard for sulfur isotope analysis sessions. Every 6 to 8 Qiuling pyrite analyses were bracketed by 2 to 3 Sonora standard analyses. Instrumental bias for $\delta^{34}S$ and $\delta^{33}S$ were determined by average values and 2 standard deviation (SD) of these bracketing standard analyses. Measured ratios of $^xS/^{32}S$ (x=34, 33) are normalized by using Vienna-Cañon Diablo troilite (V-CDT) compositions ($^{34}S/^{32}S$= 0.044163, $^{33}S/^{32}S$=0.007877, Ding et al. 2001) and are calculated as "raw" δ-values, $\delta^{34}S_{raw}$ and $\delta^{33}S_{raw}$, respectively. The equations of mass-dependent fractionation of sulfur isotopes were employed:

$$\left(\delta^{x}S\right)_{sample} = \left[\frac{\left({}^{x}S/{}^{32}S\right)_{sample}}{\left({}^{x}S/{}^{32}S\right)_{VCDT}} - 1\right] \times 1000$$

Correction factor of the instrumental bias of $\delta^{34}S$ and $\delta^{33}S$ for pyrite measurements was determined using $\delta^{34}S_{raw}$ and $\delta^{33}S_{raw}$

values of bracketing analyses of Sonora ($\delta^{34}S_{VCDT}$=+1.61‰ and $\delta^{33}S_{VCDT}$=+0.83‰, Farquhar et al. 2013) as follows:

$$\alpha_{x(\mathrm{SIMS})} = \frac{1+\left(\frac{\delta^{x}S_{raw}}{1000}\right)}{1+\left(\frac{\delta^{x}S_{standard}}{1000}\right)}$$

Values of $\delta^{34}S$ and $\delta^{33}S$ of pyrite samples were calculated using measured values of pyrite samples as follows:

$$\left(\delta^{x}S\right)_{\mathrm{Sample}} = 1000 \times \left\{\left[1+\left(\delta^{x}S\right)_{\mathrm{raw(Sample)}}/1000\right]/\alpha_{x(\mathrm{SIMS})}-1\right\}$$

The Balmat pyrite standard was analyzed several times on each mount during each of two sessions, bracketing analyses of pyrite with unknown isotopic composition. The analyses of the Balmat pyrite standard were used specifically to yield a realistic estimate of external reproducibility on $\delta^{34}S_{VCDT}$ of ±0.12‰ and $\delta^{33}S_{VCDT}$ of ±0.16‰ (2SD). The measurements of Balmat pyrite standard during the course of this study yield the value of $\delta^{34}S_{VCDT}$ ranging from +16.05 to +16.36‰ (n= 92), which within error is consistent with the reported bulk values of 16.30±0.38 and 16.39±0.40‰ (2SD) (UWPy-1 pyrite SIMS reference material at the University of Wisconsin; Kozdon et al. 2010) and grain values of 16.12±0.68‰ (2SD) (Balmat pyrite SIMS reference material at the Swedish Museum of Natural History; Whitehouse 2013).

Results

Chemical composition of pyrite

Electron microprobe results are listed in ESM 2. Arsenic is the most abundant minor element in pyrite, with concentrations ranging from 0.06 to 1.28 wt% in Py1, 0.23 to 9.59 wt% in Py2, and 0 to 0.13 wt% in Py3 (ESM 2). Arsenic has a strong inverse correlation with S (Fig. 4a). Pb, Cu, and Zn were detected in each type of pyrite. Lead is mostly in the range of 0.06–0.50 wt%, with one spot analysis revealing concentration

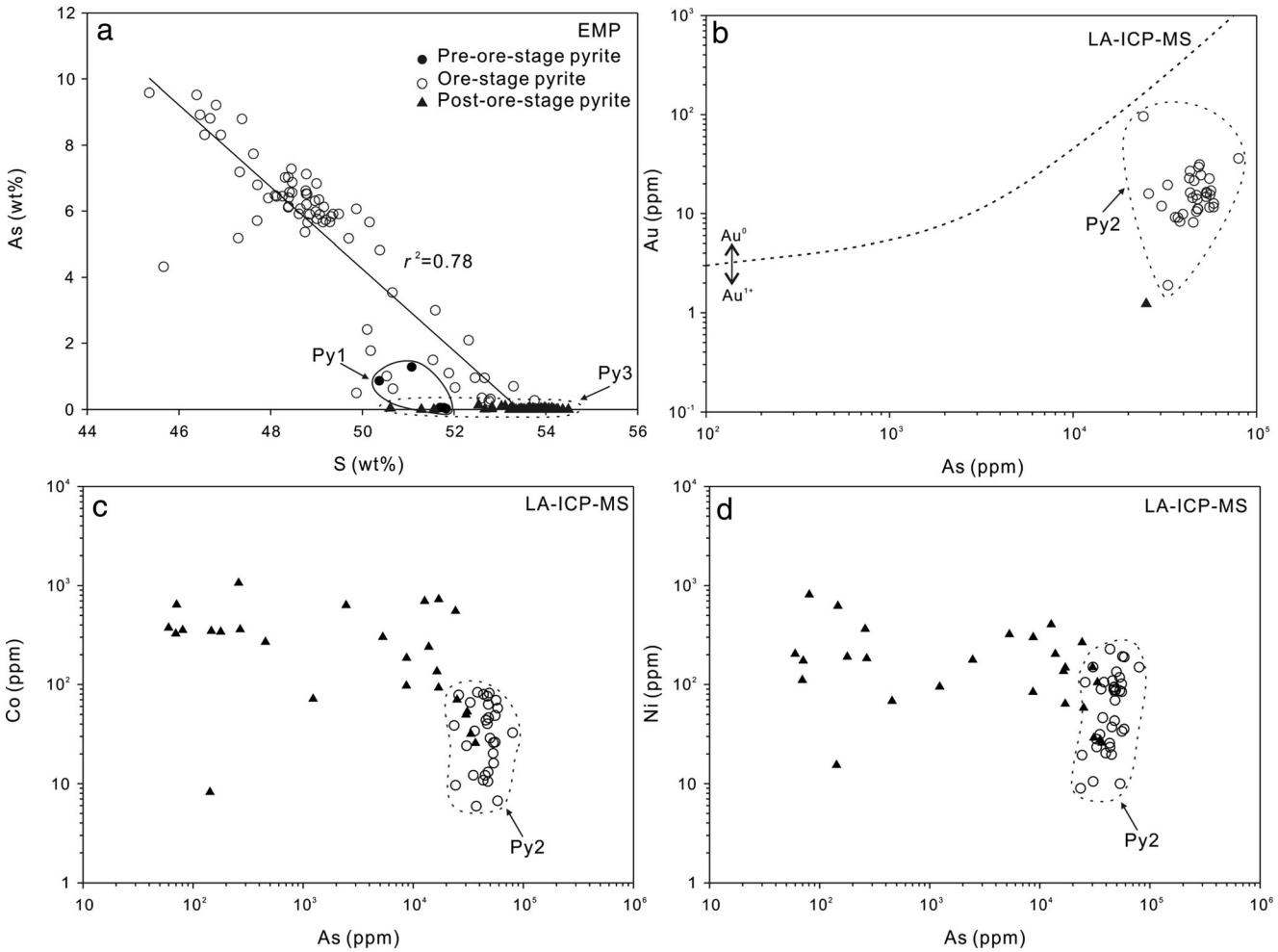

Fig. 4 Elemental abundance diagrams for pyrite. **a** As vs. S plot. **b** Au vs. As plot. The *dashed curve* represents the solubility limit of native gold in arsenian pyrite determined by Reich et al. (2005). Data points above the line contain Au^0 (particulate), whereas samples below the line contain Au^{1+} (solid solution). **c** As vs. Co plot. **d** As vs. Ni plot

up to 2.36 wt%. Cu and Zn range from 0 to 0.14 wt% and 0 to 0.05 wt%, respectively (ESM 2). Copper is more abundant in Py2 (<0.14 wt%) than in Py1 and Py3 (<0.04 wt%).

LA-ICP-MS results are reported in ESM 3. Aggregates of Py1 are generally <10–20 μm in size (Fig. 3a), which is too small to be precisely analyzed by the LA-ICP-MS method. Py2 has high and variable gold concentrations ranging from 1.0 to 96.1 ppm. Au and As data for Py2 plot well below the solubility limit for gold in arsenian pyrite (Reich et al. 2005), indicating that gold occurs as Au^{1+} in the pyrite lattice (Fig. 4b). Silver is low in Py2 (<7.9 ppm) and Au/Ag ratios range from 0.3 to 7.7. In addition, Py2 has 18.6–521 ppm Sb, 0–31 ppm Bi, 0–3.2 ppm Tl, 0–27.6 ppm Co, and 9–228 ppm Ni. Compared to Py2, Py3 is low in Au (<1.2 ppm), Sb (<413 ppm), Bi (<6.3 ppm), and Tl (below the detection limit) and high in Co (up to 210 ppm) and Ni (up to 1250 ppm; Figs. 4c, d). None of these elements show a significant correspondence with Au or Ag.

Sulfur isotopes

We analyzed 8 Py1 grains, 69 Py2 grains, and 60 Py3 grains. SIMS spot analyses results are listed in ESM 2. All of the data plots on the mass-dependent fractionation line ($\delta^{33}S = 0.515 \times \delta^{34}S$; Hulston and Thode 1965). Sulfur isotopic compositions extend from −27.1 to +69.6‰ (Fig. 5a). In more details, each type of pyrite has a distinct range of sulfur isotopic compositions as follows: −27.1 to −7.6‰ for Py1, +8.1 to +15.2‰ for Py2, and +37.4 to +69.6‰ for Py3 (Fig. 5a).

Most Py2 grains are chemically and isotopically zoned. The overlap in arsenic contents and $\delta^{34}S$ values of dark cores and As-deficient zones in the rims (Fig. 5b) confirms that the cores are correctly classified as Py2. In sample QL114 (Fig. 6a), Py2 has an As- and Au-deficient core with low $\delta^{34}S$ values of +9.3‰ that is surrounded by an As- and Au-rich rim with $\delta^{34}S$ values of +14.0 to +14.4‰ (Fig. 6a).

Py3 is unusually enriched in ^{34}S, with $\delta^{34}S$ values ranging from +37.4 to +69.6‰ (ESM 2). Grain-scale variations in sulfur isotopic compositions are also noticeable in Py3. For example, six SIMS spot analyses on one Py3 grain yielded $\delta^{34}S$ values of +39.9 to +58.7‰, which decrease abruptly by 19‰ in the outer zone (Fig. 6b).

Discussion

Field, paragenetic, textural, compositional, and S isotope data indicate that there are three types of pyrite in the Qiuling gold deposit that formed in distinct paragenetic stages: pre-ore framboidal pyrite (Py1), ore-stage fine-grained pyrite (Py2), and post-ore coarse-grained pyrite (Py3). The distinct trace elements and sulfur isotopic compositions of these three types of pyrite (Figs. 4 and 5) provide valuable information on the source and evolution of sulfur in hydrothermal fluids.

Origin of framboidal pyrite

Framboidal pyrite (Py1) mainly occurs in black shales and siltstones of the Devonian Nanyangshan Formation but is also present in some layers of the Carboniferous Yuanjiagou Formation. It commonly forms spherical aggregates consisting of discrete euhedral microcrystallites (Fig. 3a) that are likely synsedimentary or diagenetic in origin. Framboidal Py1 has low As, Cu, Co, and Ni concentrations and the lowest $\delta^{34}S$ values (ESM 2). Such diagenetic or synsedimentary pyrite is widely recognized in Paleozoic sedimentary rocks in the Qinling orogen and South China (Chang and Chu 2011).

The Py1 grains are characterized by significant enrichment in ^{32}S, with $\delta^{34}S$ values of −27.1 to −7.6‰ (ESM 2 and Fig. 5a). Such low $\delta^{34}S$ values require larger fractionations than those commonly attributed to bacterial reduction of marine sulfate with $\delta^{34}S$ values of 15–25‰ in an open system (Canfield 2001) but are still within the range of fractionations found in natural settings or documented in the laboratory (Wortmann et al. 2001; Sim et al. 2011). The lowest $\delta^{34}S$ values in Py1 may reflect the combined effects of bacterial reduction and sulfur disproportionation, which requires intermediate oxidative steps that commonly occur in shallow marine sedimentary environments (Canfield and Thamdrup 1994; Habicht and Canfield 1997; Ries et al. 2009) in which the Nanyangshan and Yuanjiagou Formations were deposited. Sulfur disproportionation can increase sulfur isotope fractionations by 4 to 5‰ under abiotic conditions (Fry et al. 1988) and up to 18‰ in biotic processes (Kaplan and Rittenberg 1964).

Source of sulfur in ore fluids

Compared to Py1 and Py3, Py2 is significantly enriched in Au, As, Cu, Sb, Tl, and Bi (ESM 2, 3), indicating its formation during the main stage of gold mineralization. Most Py2 grains are texturally and compositionally zoned (Figs. 3b and 6a). The core is generally low in As and Au, whereas the rims contain up to 9.59 wt% As and 96.1 ppm Au (ESM 2, 3). This pattern indicates that Au was transported and precipitated together with As in the ore fluids and that the core and rims may have precipitated from compositionally different hydrothermal fluids. Trace element compositions are also variable within the rims, likely having been caused by fluid-rock interactions, changes in temperature of the ore fluids, and/or alteration of earlier growth zones by evolving hydrothermal fluids (Deditius et al. 2014). Some researchers have proposed that the Au-deficient core of Py2 was formed during the sedimentary and/or diagenetic process, whereas the rims were precipitated from ore-forming fluids (Zhang et al. 1993). If this were the case, the core should

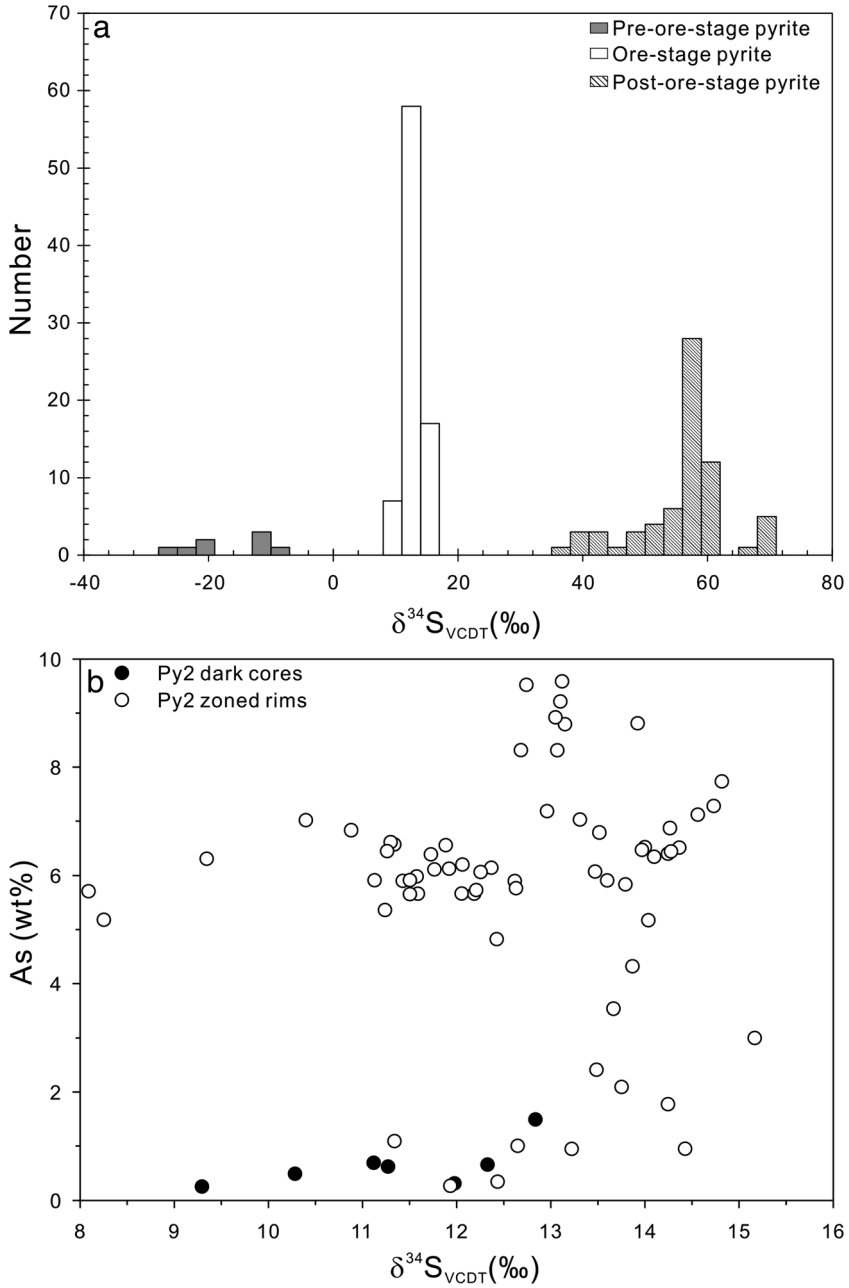

Fig. 5 **a** Histogram of $\delta^{34}S$ values for each pyrite type in the Qiuling sediment-hosted gold deposit. **b** Arsenic contents vs. $\delta^{34}S$ values plot for dark cores and zoned rims of Py2

have trace element concentrations and sulfur isotopic compositions that are consistent with Py1. However, the core of Py2 (e.g., spot A in Fig. 6a) has high Cu (0.04 wt%) and a positive $\delta^{34}S$ value (9.3‰), in sharp contrast with the framboidal Py1 that has no Cu and highly negative $\delta^{34}S$ value (−27.1 to −7.6 ‰). This geochemical contrast excludes a diagenetic origin and suggests that the core of Py2 precipitated during an early Au- and As-poor part of the ore stage.

The $\delta^{34}S$ values of hydrothermal Py2 have a relatively narrow range from +8.1 to +15.1‰, with a mode at +12.8 ‰. During the ore-stage pyrite precipitation, the temperature, fO_2, and pH of the ore-forming fluid was 250 °C, −40.2, and 5.48, respectively (Zhang and Shen 1996). In this case, the aqueous sulfur species in the ore fluid at Qiuling is dominated by H_2S (X_{H_2S} >0.90; Ohomoto 1972). The bulk sulfur isotopic composition in hydrothermal fluids is equal to or slightly lower ($\Delta^{34}S_{pyrite\text{-}fluid}$=0~+1.5‰) than the measured pyrite value (Ohmoto 1972; Chu et al. 1984). The average $\delta^{34}S_{\Sigma S\text{-}fluids}$ of +11.3~12.8‰ is significantly higher than the values of Py1 (−27.1 to −7.6‰). The large difference in the sulfur isotopic compositions between Py2 and Py1 indicates that it is unlikely that sulfur in the ore fluids was derived from the diagenetic pyrite in the Paleozoic marine sedimentary rocks, either by dissolution of Py1 or its transformation to pyrrhotite

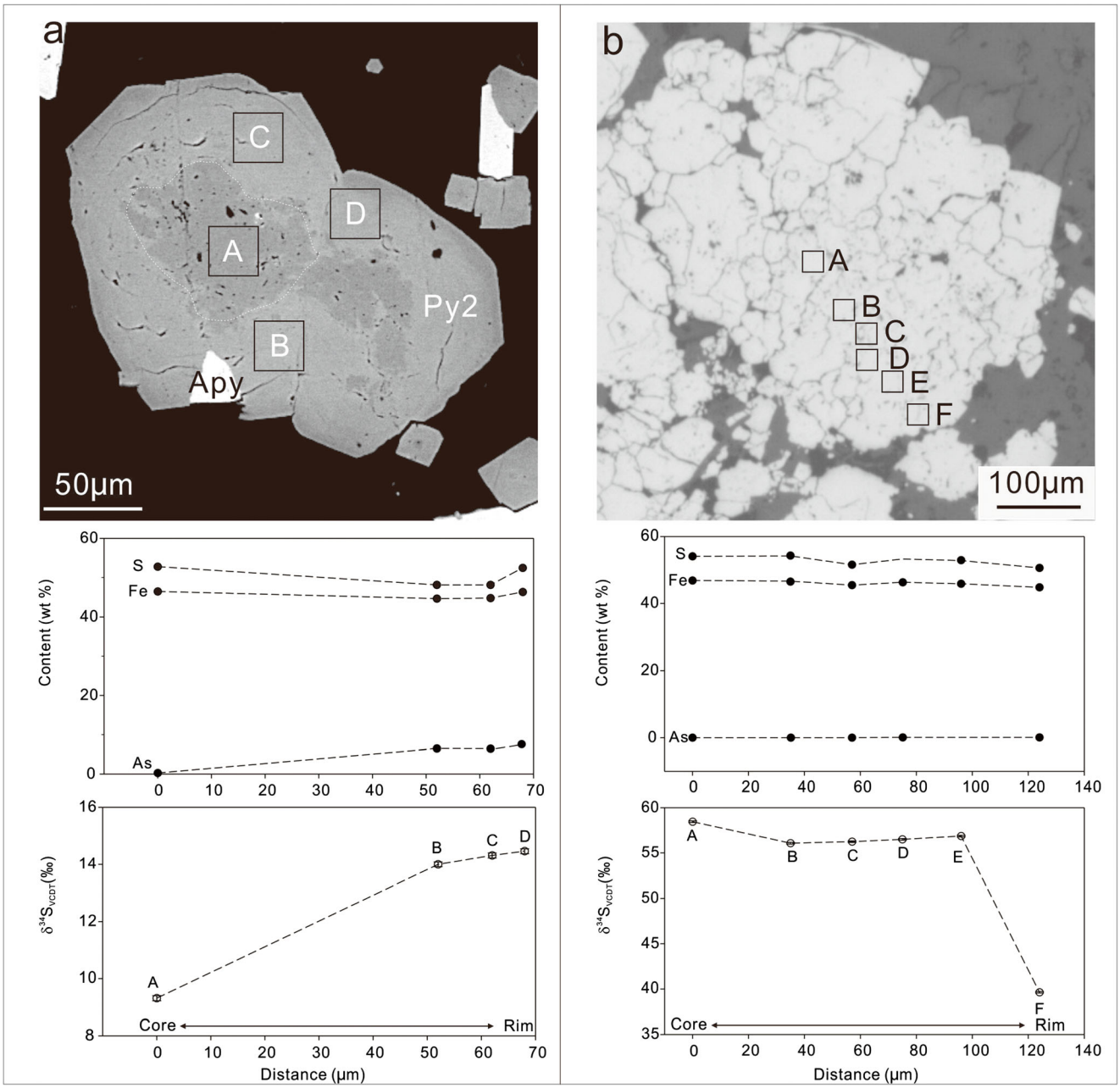

Fig. 6 **a** Backscattered electron image of selected Py2 crystal and analytical targets (indicated with *squares*) where major elements and $\delta^{34}S$ values were collected. Arsenic contents and $\delta^{34}S$ values increase from core to rim in this crystal. **b** Reflected-light photograph of selected Py3 grain and analytical targets (indicated with *squares*) where major elements and $\delta^{34}S$ values were collected. While the chemical composition is relatively constant, the $\delta^{34}S$ value drops abruptly in the rim

during regional metamorphism as documented elsewhere (Large et al. 2011). The sulfur isotopic compositions of Py2 are also distinctly different from magmatic sulfur (0±5‰; Ohmoto and Rye 1979), despite the fact that Triassic granitoid intrusions are widespread in the West Qinling orogen (Fig. 1b, c). Although magmas can assimilate sedimentary S and cycle it into hydrothermal systems to yield anomalously high or low $\delta^{34}S$ values, such values have not been reported in any of the magmatic hydrothermal system in the Qinling orogen (Zhang et al. 1997). The absence of plutons or dikes in the Qiuling mine further suggests that magmatic-derived fluid is a less likely source for the sulfur. Rather, the narrow range and positive $\delta^{34}S$ values of Py2 suggest that H_2S was most likely derived from a homogenous reservoir at deeper levels in the West Qinling orogen. Prograde metamorphism of the underlying pyritic sedimentary sequences may have produced H_2S forming the auriferous Py2 by desulfidation of pyrite to pyrrhotite and/or reduction of sulfate to sulfide by thermochemical or inorganic reactions. This view is supported by the fact that ore pyrite of many Devonian rock hosted

mesozonal orogenic gold veins in the West Qinling orogen have sulfur isotopic compositions comparable to the values of Qiuling, such as the Baguamiao gold deposit with an average $\delta^{34}S$ of +11.3‰ (Wei et al. 1994). The $\delta^{34}S$ values of ore-stage sulfides from the Baguamiao gold deposit are similar to those of diagenetic pyrite from the Upper Devonian sub-greenschist facies clastic rocks hosting gold mineralization (Wu et al. 2013), indicating that sulfur was sourced from the Devonian sedimentary rocks and their equivalents at depth during regional metamorphism.

Source of sulfur in post-ore fluid

Coarse-grained Py3 has low As and Au, high Co and Ni (Fig. 4), and extremely high $\delta^{34}S$ values ranging from +37.4 to +69.6‰ with a mode of 59.2‰ (Fig. 5a). These values are much higher than those in Py2 and have not been reported in any sediment-hosted gold deposits elsewhere in the world. The distinct differences in the textural, chemical, and isotopic characteristics of Py3 and Py2 suggest that they precipitated from discrete fluids.

One may interpret the large magnitude and spread in Py3 $\delta^{34}S$ values in terms of H_2S generated by bacterial SO_4^{2-} reduction in a system becoming close to SO_4^{2-}. However, it is unlikely that microbial activity could occur in the range of 130 to 180 °C, the temperature of post-ore hydrothermal fluid inferred from fluid inclusion microthermometry (Zhang and Shen 1996). Although the Lower Cambrian sequences in the South Qinling belt contains numerous barite beds with $\delta^{34}S$ values ranging from +38.6 to +71.8‰ (Wang and Li 1991; Wang et al. 1993; Johnson et al. 2009) similar to values of Py3 at Qiuling, no supporting evidence exists that the barite has contributed to sulfur in hydrothermal fluids from which Py3 precipitated as barite is hard to be dissolved and decomposed at low to medium temperatures. In other words, thermochemical reduction of the SO_4^{2-} from the Cambrian barite cannot explain the unusually high $\delta^{34}S$ of the Py3. Hydrogen and oxygen isotopic compositions of ore-forming fluids (Zhang et al. 2002) indicate that the Py3-forming fluids were likely derived from the formation of water contained in the Cambrian rocks. The fluids carried sulfate preferentially enriched in heavier S isotope and provided the source for sulfur forming the post-ore pyrite with large positive $\delta^{34}S$ values. The potential sources of the sulfate include Devonian evaporite and associated metalliferous black shales in underlying rocks (Yang 1991), as well as connate waters locked in the Paleozoic sedimentary rocks in the Qinling orogen. Further studies are needed to tightly constrain the source of sulfur related to Py3.

Microscopic $\delta^{34}S$ variations

To the best of our knowledge, Qiuling has the largest range of sulfur isotopic compositions ($\delta^{34}S$=−27.1 to +69.6‰) ever documented in a single sediment-hosted gold deposit. While Py1, Py2, and Py3 have distinct sulfur isotopic compositions (Fig. 5a), individual grains from the ore and post-ore-stage pyrite also show significant variation in sulfur isotopes, which would not have been revealed by conventional analytical methods using bulk pyrite samples. For example, one Py2 grain has progressively higher $\delta^{34}S$ values from the core to the outer rim from +9.3 to +14.4‰ (Fig. 6a). It is noted that the increase in $\delta^{34}S$ values of Py2 commonly occur in the rims of individual grains and are coupled with an increase in Au and As concentration in these areas. Such variations may reflect mixing of auriferous metamorphic fluids enriched in ^{34}S with pre-existing system that is Au- and ^{34}S-deficient. The narrow variation in $\delta^{34}S$ values of gold-bearing Py2 rims may indicate constant physicochemical conditions during the main ore stage. This view in turn indicates that temperature and pressure drop have not been the predominant mechanism for gold mineralization. Rather, fluid-rock interaction and fluid mixing could have been important in gold deposition. Similarly, the outer rim of a Py3 grain has a $\delta^{34}S$ value that is about 19‰ lower than values of the core and inner rims (Fig. 6b). The reason for the abrupt decrease in $\delta^{34}S$ in the rim (Fig. 6b) is currently unknown but likely reflects fluid-rock interaction and/or mixing of the ore-forming fluids with significant amounts of meteoric waters.

Conclusions

Results from this study confirm the importance of in situ microanalysis in precisely constraining source of sulfur in sediment-hosted gold deposits. The Qiuling sediment-hosted gold deposit contains three generations of pyrite (Py1, Py2, and Py3) that are texturally, chemically, and isotopically distinct. The framboidal texture and negative $\delta^{34}S$ values (−27.1 to −7.6‰) of Py1 are consistent with its formation via bacterial reduction of marine sulfate during sedimentation or early diagenesis. The narrow range of positive $\delta^{34}S$ values (+8.1 to +15.2‰) in ore-stage Py2, which are comparable to orogenic gold deposits at mesozonal levels in the neighboring areas, indicates that sulfur in the ore-forming fluids was largely sourced from metamorphic devolatization of the underlying Paleozoic marine sedimentary rocks. The extremely high $\delta^{34}S$ values (+37.4 to +69.6‰) of post-ore Py3 were likely produced by thermochemical reduction of SO_4^{2-} that was sourced from evaporite sulfate in underlying black shales or sulfate-bearing connate water locked in Paleozoic sedimentary rocks with very high $\delta^{34}S$ values (e.g., the Cambrian sequence). The grain-scale textural, chemical, and S isotopic variations in ore-stage Py2 may reflect the displacement of indigenous ground water by auriferous metamorphic fluids, whereas the chaotic $\delta^{34}S$ fluctuations in post-ore Py3 may reflect local controls on physical-chemical conditions and introduction of isotopically

light components, presumably meteoric water, into the hydrothermal system. Because the host rocks of the Qiuling gold deposit only experienced very low-grade metamorphism, metamorphic derivation of the sulfur and ore fluids indicates that the Qiuling deposit is an epizonal manifestation of an orogenic gold system in the West Qinling orogen.

Acknowledgments We thank Assistant Prof. John Cliff and Prof. Matt Kilburn for generously sharing their pyrite reference material and Ms. Hong-xia Ma for her help with microanalytical sample preparation. Dr. Shu-Guang Hua and Mr. Ji-Xiang Sui provided help in the field. The manuscript benefited from detailed and constructive reviews by two anonymous reviewers, which are gratefully appreciated. We thank Profs. Rui-zhong Hu (AE) and Bernd Lehmann (Editor-in-Chief) for editorial handling and useful suggestions. This research was supported by the National Natural Science Foundation of China (Grants 41303008, 41325007, 41203016, 41072057), China Postdoctoral Science Foundation (2013 M541034), National Basic Research Program of China (2014CB440906), the Fundamental Research Funds for the Central Universities (N120401002), and the State Key Laboratory of Lithospheric Evolution, IGG-CAS.

Compliance with ethical standards This article does not contain any studies with human or animal subjects.

Conflict of interest The authors declare that they have no competing interests.

References

Canfield DE (2001) Isotope fractionation by natural populations of sulfate-reducing bacteria. Geochim Cosmochim Acta 65:1117–1124

Canfield DE, Thamdrup B (1994) The production of ^{34}S-depleted sulfide during bacterial disproportionation of elemental sulfur. Science 266: 1973–1975

Chang H, Chu X (2011) Pyrite framboids and palaeo-ocean redox condition reconstruction. Adv Earth Sci 26:475–481

Chang Z, Large RR, Maslennikov V (2008) Sulfur isotopes in sediment-hosted orogenic gold deposits: evidence for an early timing and a seawater sulfur source. Geology 36:971–974

Chen YJ, Zhang J, Zhang FX, Pirajno F, Li C (2004) Carlin and Carlin-like gold deposits in western Qinling mountains and their metallogenic time, tectonic setting and model. Geol Rev 50:134–152 **(in Chinese with English abstract)**

Chu XL, Chen JS, Wang SX (1984) Several diagrams of sulfur isotope evolution in equilibrium with hydrothermal system. Sci Geol Sin 2: 186–200 **(in Chinese with English abstract)**

Cline JS, Hofstra AH, Muntean JL, Tosdal RM, Hickey KA (2005) Carlin-type gold deposits in Nevada: characteristics and viable models. In: Hedenquist JW, Thompson JFH, Goldfarb RJ, Richards JP (eds) Economic geology 100th anniversary. Society of Economic Geologists, Inc., Littleton, pp 451–484

Crowe DE, Vaughan RG (1996) Characterization and use of isotopically homogeneous standards for in situ laser microprobe analysis of ^{34}S/^{32}S ratios. Am Mineral 81:187–193

Deditius AP, Reich M, Kesler SE, Utsunomiya S, Chryssoulis SL, Walshe J, Ewing RC (2014) The coupled geochemistry of Au and As in pyrite from hydrothermal ore deposits. Geochim Cosmochim Acta 140:644–670

Ding T, Valkiers S, Kipphardt H, De Bievre P, Taylor P, Gonfiantini R, Krouse R (2001) Calibrated sulfur isotope abundance ratios of three IAEA sulfur isotope reference materials and V-CDT with a reassessment of the atomic weight of sulfur. Geochim Cosmochim Acta 65: 2433–2437

Dong YP, Zhang GW, Lai SC, Zhou DW, Zhu BQ (1999) An ophiolitic tectonic melange first discovered in Huashan area, south margin of Qinling orogenic belt, and its tectonic implications. Sci China Ser D Earth Sci 42:292–302

Dong YP, Zhang GW, Neubauer F, Liu XM, Genser J, Hauzenberger C (2011) Tectonic evolution of the Qinling orogen, China: review and synthesis. J Asian Earth Sci 41:213–237

Emsbo P, Hofstra AH, Lauha EA, Griffin GL, Hutchinson RW (2003) Origin of high-grade gold ore, source of ore fluid components, and genesis of the Meikle and neighboring Carlin-type deposits, northern Carlin trend, Nevada. Econ Geol 98:1069–1105

Farquhar J, Cliff J, Zerkle AL, Kamyshny A, Poulton SW, Claire M, Adams D, Harms B (2013) Pathways for Neoarchean pyrite formation constrained by mass-independent sulfur isotopes. Proc Natl Acad Sci U S A 110:17638–17643

Fry B, Gest H, Hayes JM (1988) ^{34}S/^{32}S fractionation in sulfur cycles catalyzed by anaerobic bacteria. Appl Environ Microbiol 54:250–256

Goldfarb RJ, Baker T, Dube B, Groves DI, Hart CJR, Gosselin R (2005) Distribution, character, and genesis of gold deposits in metamorphic terranes. In: Hedenquist JW, Thompson JFH, Goldfarb RJ, Richards JP (eds) Economic geology 100th anniversary. Society of Economic Geologists, Inc., Littleton, pp 407–450

Goldfarb RJ, Taylor RD, Collins GS, Goryachev NA, Orlandini OF (2014) Phanerozoic continental growth and gold metallogeny of Asia. Gondwana Res 25:48–102

Groves DI, Goldfarb RJ, Robert F, Hart CJR (2003) Gold deposits in metamorphic belts: overview of current understanding, outstanding problems, future research, and exploration significance. Econ Geol 98:1–29

Habicht KS, Canfield DE (1997) Sulfur isotope fractionation during bacterial sulfate reduction in organic-rich sediments. Geochim Cosmochim Acta 61:5351–5361

Hofstra AH, Cline JS (2000) Characteristics and models for Carlin-type gold deposits. In: Hagemann S, Brown P (eds) Gold in 2000 reviews in economic geology. Society of Economic Geologists, Inc, Littleton, pp 163–220

Hofstra AH, Leventhal JS, Northrop HR, Landis GP, Rye RO, Birak DJ, Dahl AR (1991) Genesis of sediment-hosted disseminated-gold deposits by fluid mixing and sulfidation: chemical-reaction-path modeling of ore-depositional processes documented in the Jerritt Canyon district, Nevada. Geology 19:36–40

Hua SG (2012) Mineralogy, geochemistry, and geochronology of the Qiuling gold deposit, Zhen'an County, Shanxi Province (in Chinese). Dissertation, The China University of Geosciences

Hua SG, Wang LJ, Jia XF, Chen L, Li JW (2012) Occurrence and enrichment mechanism of gold in the Qiuling Carlin-type gold deposit, Zhenan County, Shaanxi Province, China. Earth Sci 37:989–1002 **(in Chinese with English abstract)**

Hulston JR, Thode HG (1965) Variations in S^{33}, S^{34} and S^{36} contents of meteorites and their relation to chemical and nuclear effects. J Geophys Res 70:3475–3484

Johnson CA, Emsbo P, Poole FG, Rye RO (2009) Sulfur- and oxygen-isotopes in sediment-hosted stratiform barite deposits. Geochim Cosmochim Acta 73:133–147

Kaplan IR, Rittenberg SC (1964) Microbiological fractionation of sulphur isotopes. J Gen Microbiol 34:195–212

Kesler SE, Riciputi LC, Ye ZJ (2005) Evidence for a magmatic origin for Carlin-type gold deposits: isotopic composition of sulfur in the Betze-Post-Screamer deposit, Nevada, USA. Mineral Deposita 40: 127–136

Kita NT, Huberty JM, Kozdon R, Beard BL, Valley JW (2011) High-precision SIMS oxygen, sulfur and iron stable isotope analyses of geological materials: accuracy, surface topography and crystal orientation. Surf Interface Anal 43:427–431

Kozdon R, Kita NT, Huberty JM, Fournelle JH, Johnson CA, Valley JW (2010) In situ sulfur isotope analysis of sulfide minerals by SIMS: precision and accuracy, with application to thermometry of similar to 3.5 Ga Pilbara cherts. Chem Geol 275:243–253

Lai SC, Zhang GW, Yang YC, Chen JY (1998) Geochemistry of the ophiolite and island arc volcanic rock in the Mianxian-Lueyang suture zone, southern Qinling and their tectonic significances. Geochimica 27:283–293 **(in Chinese with English abstract)**

Large RR, Maslennikov V, Robert F, Danyushevsky LV, Chang Z (2007) Multistage sedimentary and metamorphic origin of pyrite and gold in the giant Sukhoi Log deposit, Lena gold province, Russia. Econ Geol 102:1233–1267

Large RR, Danyushevsky LV, Hollit C, Maslennikov V, Meffre S, Gilbert S, Bull S, Scott R, Emsbo P, Thomas H, Foster J (2009) Gold and trace element zonation in pyrite using a laser imaging technique: implications for the timing of gold in orogenic and Carlin-style sediment-hosted deposits. Econ Geol 104:635–668

Large RR, Bull SW, Maslennikov VV (2011) A carbonaceous sedimentary source-rock model for Carlin-type and orogenic gold deposits. Econ Geol 106:331–358

Liu BJ, Xu XS, Xu Q, Yang ZH (1990) Devonian sedimentary environment and basin evolution in Zhashui-Zhen'an District, eastern Qinling, China. Acta Sedimentol Sin 8:3–12 **(in Chinese with English abstract)**

Liu JJ, Zheng MH, Liu JM, Su WC (2000) Geochemistry of the La'erma and Qiongmo Au–Se deposits in the western Qinling Mountains, China. Ore Geol Rev 17:91–111

Longerich HP, Jackson SE, Gunther D (1996) Laser ablation inductively coupled plasma mass spectrometric transient signal data acquisition and analyte concentration calculation. J Anal At Spectrom 11:899–904

Ma GL, Beaudoin G, Qi SJ, Li Y (2004) Geology and geochemistry of the Changba SEDEX Pb-Zn deposit, Qinling orogenic belt, China. Mineral Deposita 39:380–395

Ma GL, Beaudoin G, Zhong SJ, Li Y, Zeng ZR (2007) Geology and geochemistry of the Dengjiashan Zn-Pb SEDEX deposit, Qinling belt, China. Can J Earth Sci 44:479–492

Mao JW, Qiu YM, Goldfarb RJ, Zhang ZC, Garwin S, Ren FS (2002) Geology, distribution, and classification of gold deposits in the western Qinling belt, central China. Mineral Deposita 37:352–377

Mojzsis SJ, Coath CD, Greenwood JP, McKeegan KD, Harrison TM (2003) Mass-independent isotope effects in Archean (2.5 to 3.8 Ga) sedimentary sulfides determined by ion microprobe analysis. Geochim Cosmochim Acta 67:1635–1658

Ohmoto H (1972) Systematics of sulfur and carbon isotopes in hydrothermal ore deposits. Econ Geol 67:551–578

Ohmoto H, Rye RO (1979) Isotopes of sulfur and carbon. In: Barnes HL (ed) Geochemistry of hydrothermal ore deposits. Wiley, New York, pp 509–567

Qi SJ, Li Y (1993) Lead-zinc metallogenic belt of Devonian system in Qinling Mountains (in Chinese). Geological Publication House, Beijing

Qin JF, Lai SC, Grapes R, Diwu CR, Ju YJ, Li YF (2009) Geochemical evidence for origin of magma mixing for the Triassic monzonitic granite and its enclaves at Mishuling in the Qinling orogen (central China). Lithos 112:259–276

Ratschbacher L, Hacker BR, Calvert A, Webb LE, Grimmer JC, McWilliams MO, Ireland T, Dong SW, Hu JM (2003) Tectonics of the Qinling (central China): tectonostratigraphy, geochronology, and deformation history. Tectonophysics 366:1–53

Reich M, Kesler SE, Utsunomiya S, Palenik CS, Chryssoulis SL, Ewing RC (2005) Solubility of gold in arsenian pyrite. Geochim Cosmochim Acta 69:2781–2796

Ries JB, Fike DA, Pratt LM, Lyons TW, Grotzinger JP (2009) Superheavy pyrite ($\delta^{34}S_{pyr}>\delta^{34}S_{CAS}$) in the terminal proterozoic nama group, southern Namibia: a consequence of low seawater sulfate at the dawn of animal life. Geology 37:743–746

Saunders JA, Hofstra AH, Goldfarb RJ, Reed MH (2014) Geochemistry of hydrothermal gold deposits. In: Holland HD, Turekian KK (eds) Treatise on geochemistry, 2nd edn. Elsevier, Oxford, pp 383–424

Sim MS, Bosak T, Ono S (2011) Large sulfur isotope fractionation does not require disproportionation. Science 333:74–77

Wang ZC, Li GZ (1991) Barite and witherite deposits in lower Cambrian shales of South China: stratigraphic destribution and geochemical characterization. Econ Geol 86:354–363

Wang ZC, Chu XL, Li Z (1993) Original explanation on the high $\delta^{34}S$ values of a barite deposit. Sci Geol Sin 28:191–192 **(in Chinese with English abstract)**

Wang XX, Wang T, Castro A, Pedreira R, Lu XX, Xiao QH (2011) Triassic granitoids of the Qinling orogen, central China: genetic relationship of enclaves and rapakivi-textured rocks. Lithos 126: 369–387

Wei LM, Cao YG, Wang ML (1994) Geological characteristics and genesis analysis of Baguamiao gold deposits, Shaanxi province. In: Liu DS (ed) Chinese Carlin-type gold deposits (in Chinese). University of Nanjing Press, Nanjing, pp 286–305

Whitehouse MJ (2013) Multiple sulfur isotope determination by SIMS: evaluation of reference sulfides for $\Delta^{33}S$ with observations and a case study on the determination of $\Delta^{36}S$. Geostand Geoanal Res 37:19–33

Whitehouse MJ, Kamber BS, Fedo CM, Lepland A (2005) Integrated Pb- and S-isotope investigation of sulphide minerals from the early Archaean of Southwest Greenland. Chem Geol 222:112–131

Wilson SA, Ridley WI, Koenig AE (2002) Development of sulfide calibration standards for the laser ablation inductively-coupled plasma mass spectrometry technique. J Anal At Spectrom 17:406–409

Wortmann UG, Bernasconi S, Böttcher ME (2001) Hypersulfidic deep biosphere indicates extreme sulfur isotope fractionation during single-step microbial sulfate reduction. Geology 29:647–650

Wu B, Jiang WM, Xiong YL, Zeng XH, Li X (2013) New understanding of genesis of Baguamiao gold deposits. Resour Environ Eng 27: 339–342 **(in Chinese with English abstract)**

Xue F, Lerch MF, Kröner A, Reischmann T (1996) Tectonic evolution of the East Qinling Mountains, China, in the Palaeozoic: a review and new tectonic model. Tectonophysics 253:271–284

Yang ZH (1991) Tectonic lithofacies and mineralization of marginal transform basin (in Chinese). Science Press, Beijing

Zhai XM, Day HW, Hacker BR, You ZD (1998) Paleozoic metamorphism in the Qinling orogen, Tongbai Mountains, central China. Geology 26:371–374

Zhang GW (1988) Formation and evolution of the Qinling orogen (in Chinese). Northwest University Press, Xi'an

Zhang FX, Shen P (1996) Study on metallogenic physicochemical conditions and metallogenic mechanism of the Qiuling micro-disseminated gold deposit in Zhen'an County, Shaanxi Province. Geol Prospecting 32:8–15 **(in Chinese with English abstract)**

Zhang FX, Liu WF, Wei KY (1993) Features and evolution of Au-bearing pyrite in the Jinlongshan-Qiuling Au-deposit of Ding-Ma ore belt, Shaanxi. Geol Prospecting 29:27–33 **(in Chinese with English abstract)**

Zhang FX, Wei KY, Ma JQ (1997) Geology and prospecting of micro-disseminated (Carlin type) gold deposits in South Qinling (in Chinese). Northwest University Press, Xi'an

Zhang GW, Yu ZP, Dong YP, Yao YP (2000) On Precambrian framework and evolution of the Qinling belt. Acta Petrol Sin 16:11–21 **(in Chinese with English abstract)**

Zhang GW, Zhang BR, Yuan XC, Xiao QH (2001) Qinling orogenic belt and continental dynamics (in Chinese). Science Press, Beijing

Zhang J, Chen YJ, Zhang FX, Li C (2002) Geochemical study of ore fluid in Jinlongshan Carlin-type gold ore belt in southwestern Shaanxi province. Mineral Deposits 21:283–291 **(in Chinese with English abstract)**

Zhang CL, Wang T, Wang XX (2008) Origin and tectonic setting of the early Mesozoic granitoids in Qinling orogenic belt. Geol J China Univ 14:304–316 **(in Chinese with English abstract)**